J|A|C|S
COMMUNICATIONS

Synthesis and Oxygen Reduction Electrocatalytic Property of Pt-on-Pd Bimetallic Heteronanostructures

Zhenmeng Peng and Hong Yang*

Department of Chemical Engineering, University of Rochester, Gavett Hall 206, Rochester, New York 14627

Received March 22, 2009; E-mail: hongyang@che.rochester.edu

One key area in advancing hydrogen fuel cells is to improve both the sluggish kinetics and long-term stability of cathode catalysts.[1−3] A major strategy for improving the activity is to use platinum alloys instead of pure platinum as the electrocatalysts,[4] though leaching of nonplatinum metal over time is a major issue. The loss of surface area due to Ostwald ripening or grain growth is another major factor that often results in the degradation of catalytic performance.[5] One solution to improve the durability is to deposit Au nanoclusters on Pt catalysts.[6]

In this paper, we describe a new approach to address both the activity and stability issues synergistically by using palladium metal nanoparticles as support for Pt catalysts based on a particle-on-particle structure. Such heterogeneous bimetallic nanocrystals are expected to integrate several different functionalities in one structure, which is difficult to accomplish in a single-component material. The rationales for choosing palladium as a metallic support for platinum nanoparticles are based on the following two major factors: First, both metals have a face-centered cubic (*fcc*) phase with a unit length of 3.92 Å for Pt and 3.89 Å for Pd. The small lattice mismatch means that the epitaxial growth should be favored.[7] Second, a Pt monolayer on a Pd surface shows significantly higher catalytic activity than pure Pt in an oxygen reduction reaction (ORR).[8]

Selective growth of metals on semiconductors and metal oxides and semiconductors on semiconductors has been investigated in recent years, though examples on well-defined metal-on-metal heteronanostructures are still quite limited.[7,9−11] Heterogeneous nucleation and growth, however, should be favored thermodynamically over the homogeneous nucleation for the corresponding individual elements, when the global energy minimum is dominated by interfacial energy.[3,12] Additional reduction in free energy can further be achieved through epitaxial growth. Here we report the synthesis of Pt-on-Pd heterogeneous bimetallic nanostructures based on such principles. Carbon-supported Pt-on-Pd bimetallic nanostructures are further examined for its catalytic properties in ORR.

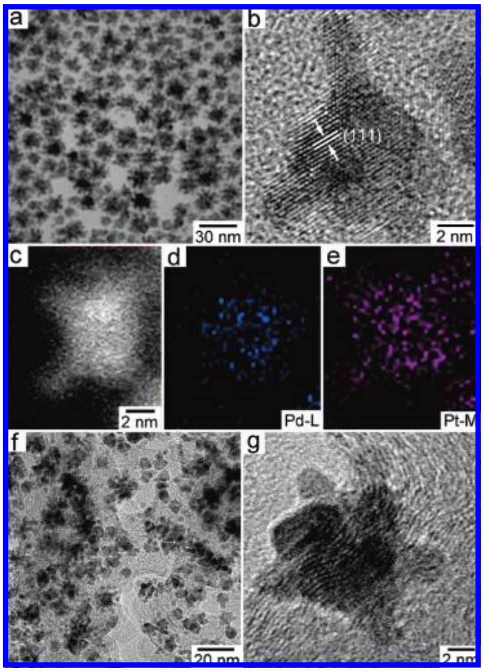

Figure 1. Representative (a) TEM, (b) HR-TEM, (c) HAADF-STEM images and (d, e) elemental maps for Pd and Pt metals of Pt-on-Pd bimetallic nanoparticles; (f) TEM and (g) HR-TEM images of carbon-supported Pt-on-Pd bimetallic catalysts after the thermal treatments.

The Pt-on-Pd nanoparticles were prepared using a sequential synthetic method (See Supporting Information for details). The palladium nanoparticles were made from palladium acetylacetonate in oleylamine based on a modified procedure.[13,14] The as-made palladium nanoparticles were fairly monodisperse and had an average diameter of 5.3 ± 0.6 nm (Figure S1). A powder X-ray diffraction (PXRD) pattern shows the particles were made of Pd metal (Figure S2). Figure 1a shows the representative TEM image for the as-synthesized Pt-on-Pd nanoparticles. The Pt nanoparticles had an average diameter of ~3 nm and were distributed evenly on the surface of palladium nanoparticles. A high-resolution TEM (HR-TEM, FEI TECNAI F-20) image shows that these nanoparticles have good crystallinity with well-defined fringes (Figure 1b). The Pt nanoparticles grew along the (111) crystal planes on Pd supports. No obvious grain boundaries or defects could be observed, as only a very small lattice mismatch of 0.77% existed between Pt and Pd metals.[7] Similar architectures have been reported in other bimetallic systems, such as Au−Pt.[11] The elemental distributions of these two metals were studied by high-angle annular dark field scanning TEM (HAADF-STEM). Figure 1c−e show a representative STEM image and the corresponding energy dispersive X-ray (EDX) maps for Pd and Pt of a Pt-on-Pd nanoparticle. While Pd could only be detected in the core region, Pt was found throughout the entire particle including the "branch" regions, indicating the formation of Pt-on-Pd nanoparticles. A PXRD pattern shows multiple diffraction peaks could be observed and indexed to an *fcc* lattice (Figure S2). The atomic ratio between Pd and Pt in the bimetallic nanostructures was ~1/3 based on the EDX analysis using field emission scanning electron microscopy (FE-SEM, Zeiss-Leo DSM982), close to the Pd metal/Pt(acac)$_2$ molar ratio in the reaction mixture (Figure S3). The as-made nanoparticles could be loaded onto a carbon support (Vulcan XC-72R) and thermally treated to make Pt-on-Pd bimetallic catalysts. Figure 1f shows representative TEM images of carbon-supported Pt-on-Pd nanoparticles at 20 wt % loading of metals. The Pt-on-Pd nanoparticles were still evenly distributed on carbon supports without obvious sintering or growth of particles after thermal treatment. HR-TEM study and EDX maps show the particle-on-particle morphology and elemental distributions remained largely intact (Figure 1g and Figure S4a−c). The

10.1021/ja902256a CCC: $40.75

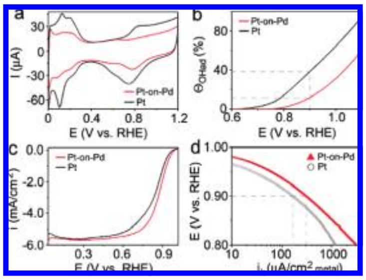

Figure 2. (a) CV, (b) hydroxyl surface coverage (Θ_{OH}), (c) ORR polarization curves, and (d) specific kinetic current densities (i_k) for carbon-supported Pt-on-Pd and Pt catalysts.

PXRD diffraction peaks became slightly sharper than before (Figure S4d), indicating an improvement in crystallinity.

Figure 2 shows the electrochemical properties of carbon-supported Pt-on-Pd heteronanostructure and Pt reference catalysts (E-TEK, 20 wt % Pt, diameter: 2.5 nm) (See Supporting Information for details). The electrochemical surface area (ECSA) for the Pt-on-Pd catalyst was found to be 37.3 m^2/g metal (or 44.5 m^2/g Pt) based on the cyclic voltammetry (CV) data (Figure 2a). Well-defined chemical adsorption peaks of hydrogen on different Pt low-index surfaces became less definable for the Pt-on-Pd catalyst. The incorporation of Pd also greatly altered the ability to absorb hydroxyl species (OH_{ad}, $E > 0.6$ V) (Figure 2b). Both the onset and peak potentials for the Pt-on-Pd catalyst had positive shifts in comparison with pure Pt on the backward sweep, suggesting the fast hydroxyl desorption from the Pt-on-Pd surfaces. The ORR tests were conducted in O_2-saturated $HClO_4$ aqueous solutions at an ECSA of 2.0 cm^2 for all catalysts on a glass carbon electrode (GCE). Figure 2c shows the polarization curves for both carbon-supported Pt-on-Pd and pure Pt catalysts. The Pt-on-Pd catalysts exhibited a more positive on-set potential and higher activity than the pure Pt nanoparticles. The area-specific current density (i_k), which represents the intrinsic activity of the catalysts and calculated using Koutecky−Levich equation,[15] was 307 μA/cm^2 Pt at 0.9 V for the Pt-on-Pd nanostructures and nearly doubled that for the Pt catalyst (166 μA/cm^2 metal) (Figure 2d). These results agreed well with those reported for Pt skin layers on Pd surfaces.[8] The adsorbed OH_{ad} species has a negative impact on the ORR and low OH_{ad} coverage on the surface of Pt-on-Pd catalysts helps improve the kinetics, thus enhancing the activities.[3,8]

The long-term stability of the Pt-on-Pd catalyst was evaluated by applying linear potential sweeps between 0.6 and 1.0 V based on an established procedure.[5a,6] After 30 000 cycles, Pt-on-Pd catalysts lost ∼12% of the initial ECSA (Figure 3a) and showed a small degradation of 9 mV in the half-wave potential (Figure 3b). The particle-on-particle morphology, size, and even composition remained after the accelerated tests (Figure S5). In sharp contrast, the degradation of Pt catalyst was quite serious, with a loss of 39% of the initial ECSA and a large decrease of 35 mV in the half-wave potential after the test (Figure 3c−d). The Pt nanoparticles also experienced a dramatic growth in diameter after the cycles, changing from 2.5 to 3.9 nm (Figure S6). The much improved stability thus could be due to the favored interfacial structures between Pt and Pd supports, as well as the larger than usual overall particle size of Pt-on-Pd nanostructures, which prevented the small Pt from dissolution in the ORR. This platinum-on-metal architecture provides a new design strategy for making hydrogen fuel cell cathode catalysts with both excellent activity and stability.

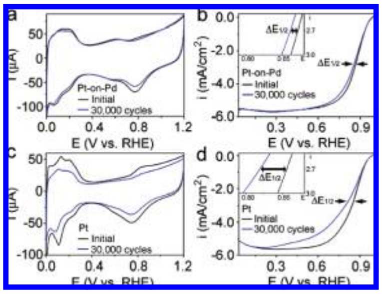

Figure 3. CV and ORR polarization curves for carbon-supported (a, b) Pt-on-Pd and (c, d) Pt catalysts before and after 30 000 cycles.

Acknowledgment. This work is supported by the NSF (DMR-0449849). It made use of Shared Facilities at University of Rochester River Campus EM Lab supported in part by the DOE.

Supporting Information Available: Detailed synthesis and characterization procedures. Figures S1−S6 contain TEM, XRD, EDX, electrochemical activity, and stability data. This material is available free of charge via the Internet at http://pubs.acs.org.

References

(1) (a) Gasteiger, H. A.; Kocha, S. S.; Sompalli, B.; Wagner, F. T. *Appl. Catal., B* **2005**, *56*, 9–35. (b) de Bruijn, F. A.; Dam, V. A. T.; Janssen, G. J. M. *Fuel Cells* **2008**, *8*, 3–22.
(2) Chen, G. Y.; Delafuente, D. A.; Sarangapani, S.; Mallouk, T. E. *Catal. Today* **2001**, *67*, 341–355.
(3) Peng, Z. M.; Yang, H. *Nano Today* **2009**, *4*, 143–164.
(4) (a) Stamenkovic, V. R.; Fowler, B.; Mun, B. S.; Wang, G. F.; Ross, P. N.; Lucas, C. A.; Markovic, N. M. *Science* **2007**, *315*, 493–497. (b) Koh, S.; Strasser, P. *J. Am. Chem. Soc.* **2007**, *129*, 12624–12625. (c) Chen, S.; Ferreira, P. J.; Sheng, W. C.; Yabuuchi, N.; Allard, L. F.; Shao-Horn, Y. *J. Am. Chem. Soc.* **2008**, *130*, 13818–13819. (d) Stamenkovic, V.; Schmidt, T. J.; Ross, P. N.; Markovic, N. M. *J. Phys. Chem. B* **2002**, *106*, 11970–11979.
(5) (a) Ferreira, P. J.; la O, G. J.; Shao-Horn, Y.; Morgan, D.; Makharia, R.; Kocha, S.; Gasteiger, H. A. *J. Electrochem. Soc.* **2005**, *152*, A2256–A2271. (b) Shao, Y. Y.; Yin, G. P.; Gao, Y. Z. *J. Power Sources* **2007**, *171*, 558–566. (c) Yu, X. W.; Ye, S. Y. *J. Power Sources* **2007**, *172*, 145–154.
(6) Zhang, J. L.; Sasaki, K.; Sutter, E.; Adzic, R. R. *Science* **2007**, *315*, 220–222.
(7) (a) Habas, S. E.; Lee, H.; Radmilovic, V.; Somorjai, G. A.; Yang, P. *Nat. Mater.* **2007**, *6*, 692–697. (b) Lee, H. J.; Habas, S. E.; Somorjai, G. A.; Yang, P. D. *J. Am. Chem. Soc.* **2008**, *130*, 5406–5407.
(8) (a) Zhang, J. L.; Mo, Y.; Vukmirovic, M. B.; Klie, R.; Sasaki, K.; Adzic, R. R. *J. Phys. Chem. B* **2004**, *108*, 10955–10964. (b) Zhang, J. L.; Vukmirovic, M. B.; Xu, Y.; Mavrikakis, M.; Adzic, R. R. *Angew. Chem., Int. Ed.* **2005**, *44*, 2132–2135.
(9) (a) Mokari, T.; Rothenberg, E.; Popov, I.; Costi, R.; Banin, U. *Science* **2004**, *304*, 1787–1790. (b) Mokari, T.; Sztrum, C. G.; Salant, A.; Rabani, E.; Banin, U. *Nat. Mater.* **2005**, *4*, 855–863. (c) Yu, H.; Chen, M.; Rice, P. M.; Wang, S. X.; White, R. L.; Sun, S. H. *Nano Lett.* **2005**, *5*, 379–382. (d) Cozzoli, P. D.; Manna, L. *Nat. Mater.* **2005**, *4*, 801–802. (e) Gu, H. W.; Zheng, R. K.; Zhang, X. X.; Xu, B. *J. Am. Chem. Soc.* **2004**, *126*, 5664–5665. (f) Yang, J.; Elim, H. I.; Zhang, Q. B.; Lee, J. Y.; Ji, W. *J. Am. Chem. Soc.* **2006**, *128*, 11921–11926.
(10) Milliron, D. J.; Hughes, S. M.; Cui, Y.; Manna, L.; Li, J. B.; Wang, L. W.; Alivisatos, A. P. *Nature* **2004**, *430*, 190–195.
(11) (a) Peng, Z. M.; Yang, H. *Nano Res.* **2009**, *2*, 406–415. (b) Zhou, S. G.; McIlwrath, K.; Jackson, G.; Eichhorn, B. *J. Am. Chem. Soc.* **2006**, *128*, 1780–1781.
(12) (a) Roder, H.; Schuster, R.; Brune, H.; Kern, K. *Phys. Rev. Lett.* **1993**, *71*, 2086–2089. (b) Wilcoxon, J. P.; Provencio, P. P. *J. Am. Chem. Soc.* **2004**, *126*, 6402–6408. (c) Chambers, S. A. *Surf. Sci. Rep.* **2000**, *39*, 105–180.
(13) Kim, S. W.; Park, J.; Jang, Y.; Chung, Y.; Hwang, S.; Hyeon, T.; Kim, Y. W. *Nano Lett.* **2003**, *3*, 1289–1291.
(14) Liu, Q. S.; Bauer, J. C.; Schaak, R. E.; Lunsford, J. H. *Angew. Chem., Int. Ed.* **2008**, *47*, 6221–6224.
(15) (a) Bard, A. J.; Faulkner, L. R. *Electrochemical Methods - Fundamentals and Application*, 2nd ed.; John Wiley & Sons:New York, 2001. (b) Vielstich, W.; Lamm, A.; Gasteiger, H. A. *Handbook of Fuel Cells, Fundametnals Technology and Applications*; John Wiley & Sons Ltd.: 2003; Vol. 2.

JA902256A

Supporting Information

Synthesis and Oxygen Reduction Electrocatalytic Property of Pt-on-Pd Bimetallic Heteronanostructures

Zhenmeng Peng, Hong Yang[*]

Department of Chemical Engineering, University of Rochester, Gavett Hall 206,

Rochester, NY 14627

* CORRESPONDING AUTHOR
E-mail: hongyang@che.rochester.edu

Telephone: (585) 275-2110; Fax: (585) 273-1348

Experimental procedure

Synthesis. Pt-on-Pd bimetallic nanoparticles were prepared by a sequential synthetic method. All the experiments were conducted under an argon atmosphere using a standard Schlenk line. In a typical procedure, palladium nanoparticles were produced first. To make Pd nanoparticles, palladium acetylacetonate ($Pd(acac)_2$, 99%, Strem, 0.1 g or 0.33 mmol) was dissolved in trioctylphosphine (TOP, 90%, Aldrich, 0.5 mL or 1.1 mmol) to form Pd-TOP complex in a 25-mL three-neck flask. Oleylamine (OAm, 70%, Aldrich, 10 mL) was then added into this flask. The resulting solution was slowly heated to 250 °C at a rate of 2 °C/min and maintained at this temperature for 30 min before cooling down to ambient room temperatures. The product was precipitated out by washing twice with a mixture of 6 mL of hexane and 18 mL of ethanol, followed by centrifugation at 6000 rpm for 10 min. The precipitate was dispersed in 4 mL of dipenyl ether (DPE, 99%, Aldrich) for the subsequent use in the preparation of Pt-on-Pd nanoparticles, which began by mixing platinum actylacetonate ($Pt(acac)_2$, 98%, Strem, 0.02 g or 50 μmol) and Pd nanoparticles (12.5 μmol in metal) in 5 mL of DPE and 0.3 mL of OAm. The concentration of Pd nanoparticles in DPE was determined by thermal gravimetric analysis (TGA) conducted on an SDT-Q600 system from TA Instruments, Inc. This mixture was heated to 180 °C and kept at this temperature for 1 h. The product was precipitated out by washing with 10 mL of ethanol, followed by centrifugation at 6000 rpm for 10 min. The precipitate was dispersed in 3 mL of hexane.

Preparation of carbon-supported Pt-on-Pd nanostructure catalysts. A suspension of 40 mg of carbon black (Vulcan® XC72R) in 2 mL of hexane was sonicated for 1 h, followed by the addition of Pt-on-Pd nanoparticles that contained 10 mg of metals. The amount of Pt-on-Pd nanoparticles in hexane was determined by TGA analysis. This mixture was stirred overnight and the resulting solid was precipitated out via centrifugation. The carbon-supported Pt-on-Pd nanoparticles were thermally treated at 300 °C for 1 h in air to remove the surface capping agents and at 80 °C for 2 h in a forming gas of H_2/Ar to ensure the surface composing of zero valence metals.

Characterization

Transmission electron microscopy (TEM) images were taken on a JEOL JEM 2000EX microscope at an accelerating voltage of 200 kV. High-resolution transmission electron microscopy (HR-TEM) images were taken on a FEI TECNAI F-20 microscope operated at 200 kV. Scanning transmission electron microscopy (STEM) and elemental maps were carried out under the high-angle annular dark field (HAADF) mode. Energy dispersive X-ray (EDX) analysis of particle ensembles was carried out on a field emission scanning electron microscope (FE-SEM, Zeiss-Leo DSM982). Powder X-ray diffraction (PXRD) patterns were recorded using a Philips MPD diffractometer with a Cu K_α X-ray source (λ=1.5405 Å). The thermal gravimetric analysis (TGA) was conducted on an SDT-Q600 system from TA Instruments, Inc.

Electrochemical properties of the catalysts were measured on a CHI 760 dual channel electrochemical workstation from CH Instruments, Inc. using a three-electrode system that consists of a glassy carbon working electrode (5 mm in diameter), a platinum leaf electrode, and a hydrogen reference electrode (HydroFlex, Gaskatel). The hydrogen reference electrode was placed in a separate cell containing 0.05-M H_2SO_4 aqueous solution and connected with the main cell using a salt bridge. The HydroFlex electrode was calibrated by performing hydrogen evolution reaction (HER) with two Pt electrodes. All the potentials were recorded with respect to a reversible hydrogen electrode (RHE).

The catalyst dispersions were prepared by mixing 5 mg of designed catalyst in 5 mL of aqueous solution containing 1 mL of iso-propanol and 25 μL of a 5 wt.% Nafion® solution (V_{water}: $V_{2\text{-}propanol}$: $V_{5\%\ Nafion}$ = 0.8: 0.2: 0.005), followed by ultrasonication for 10 min. A designed amount of dispersion was drop-cast onto the glassy carbon electrode (5 mm in diameter) and dried for 30 min before the measurements. For ECSA study, the cyclic voltammetry (CV) was conducted at catalyst loading of 2 μg of metals in an Ar-protected 0.1 M perchloric acid ($HClO_4$) aqueous solution. The scan rate was 20 mV/s. The ECSA values were calculated by integrating the area under curve in the hydrogen adsorption range between 0.05 and 0.4 V for the backward sweep in the CV. The adsorption of hydroxyl species was calculated based on the OH_{ad} peak in the CV curves at the potential larger than 0.6 V. Dividing the hydroxyl adsorption area by the overall active surface area resulted in the surface coverage of OH_{ad} species (Θ_{OHad}).

All oxygen reduction reaction (ORR) tests were conducted at ambient room temperature in O_2-saturated 0.1-M $HClO_4$ aqueous solutions. The loading was based on the ECSA of the catalysts, which were set at 2 cm^2 for all the ORR studies. The polarization curves were obtained by sweeping the potential from 0 to 1 V at the scan rate of 10 mV/s and rotation disk speed of 1600 rpm. Before recording the data, the current densities for the prepared catalysts were checked to make sure that they reached the diffusion limited of about 6 mA/cm^2 and mass-transport was not an issue in these measurements.[1,2] The Koutecky-Levich equation was applied to calculate kinetic current density based on ORR polarization curves, which can be described as follow:[3]

$$\frac{1}{i} = \frac{1}{i_k} + \frac{1}{i_d} = \frac{1}{i_k} + \frac{1}{B\omega^{1/2}} \qquad (1)$$

where, i is the measured current density, i_k is the kinetic current density, i_d is the diffusion (mass-transfer) limited current density, B is a constant and a function of concentration (C_{O2}), diffusion coefficient (D_{O2}) of O_2 in the electrolyte and viscosity of the electrolyte (ν), and ω is the rotation rate of the electrode in unit of rpm. The value obtained for kinetic current was independent of diffusion and could be used to evaluate the intrinsic activity of the catalysts. The area-specified current density (i_k) was obtained by normalizing the current based on the active surface areas of the catalysts.

The accelerated stability tests were conducted at ambient room temperature in Ar-protected 0.1-M $HClO_4$ aqueous solutions. The loading was based on the ECSA of the catalysts and set at 2 cm^2. The corresponding mass loadings of the catalysts were 5.4 μg of metal for Pt-on-Pd nanostructures and 2.4 μg of metal for Pt nanoparticles (E-TEK, 20 wt.% Pt, diameter: 2.5 nm).

The potentials were cycled continuously for 30,000 times between 0.6 and 1.0 V (vs. RHE) at a scan rate of 100 mV/s. The ECSA after stability test was calculated based on the CV curve by integrating the area for hydrogen adsorption.

References

(1) Stamenkovic, V.; Schmidt, T. J.; Ross, P. N.; Markovic, N. M. *J. Phys. Chem. B* **2002**, *106*, 11970-11979.

(2) Gasteiger, H. A.; Kocha, S. S.; Sompalli, B.; Wagner, F. T. *Appl. Catal. B-Environ.* **2005**, *56*, 9-35.

(3) Vielstich, W.; Lamm, A.; Gasteiger, H. A. *Handbook of Fuel Cells, Fundametnals Technology and Applications*; John Wiley & Sons Ltd., 2003; Vol. 2.

(4) Ferreira, P. J.; la O, G. J.; Shao-Horn, Y.; Morgan, D.; Makharia, R.; Kocha, S.; Gasteiger, H. A. *J. Electrochem. Soc.* **2005**, *152*, A2256-A2271.

(5) Zhang, J. L.; Sasaki, K.; Sutter, E.; Adzic, R. R. *Science* **2007**, *315*, 220-222.

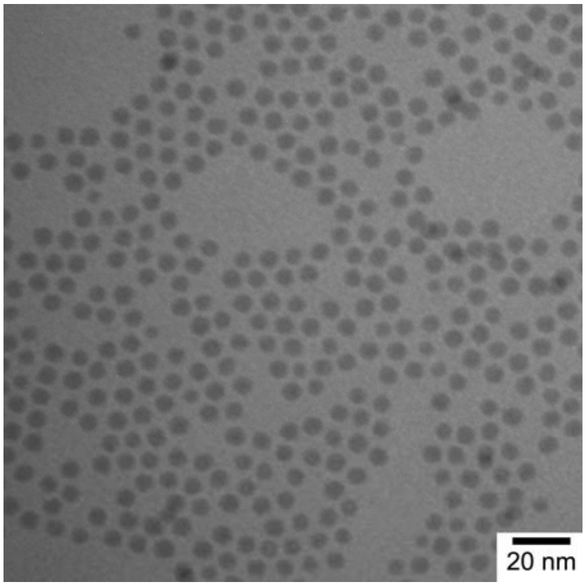

Figure S1. Representative TEM image of as-synthesized Pd nanoparticles.

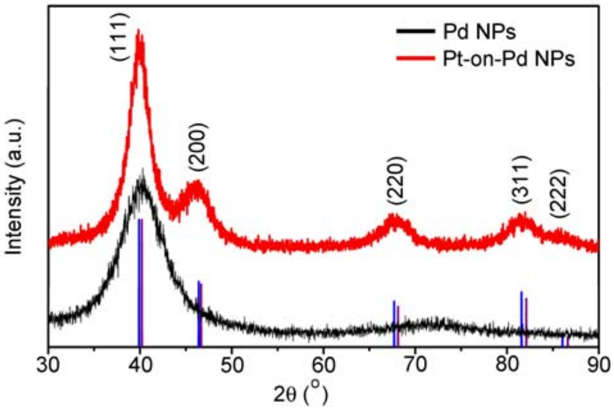

Figure S2. Powder X-ray diffraction (PXRD) patterns of as-prepared Pd and Pt-on-Pd nanoparticles. The intensity and position for Pt (blue) and Pd (purple) references were taken from the JCPDS database.

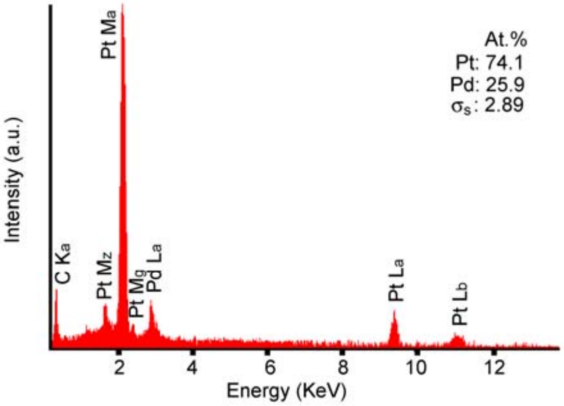

Figure S3. Energy dispersive X-ray (EDX) spectrum of as-prepared Pt-on-Pd nanoparticles collected on a field emission scanning electron microscope (FE-SEM, Zeiss-Leo DSM982).

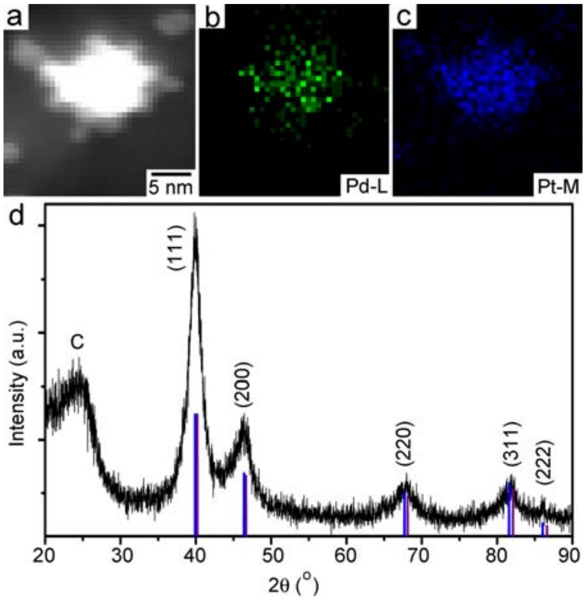

Figure S4. Representative (a) HAADF-STEM image and (b, c) the corresponding elemental maps of Pd and Pt metals, and (d) PXRD pattern of carbon-supported Pt-on-Pd bimetallic nanoparticles after the thermal treatments. The intensity and position for Pt (blue) and Pd (purple) references were taken from the JCPDS database.

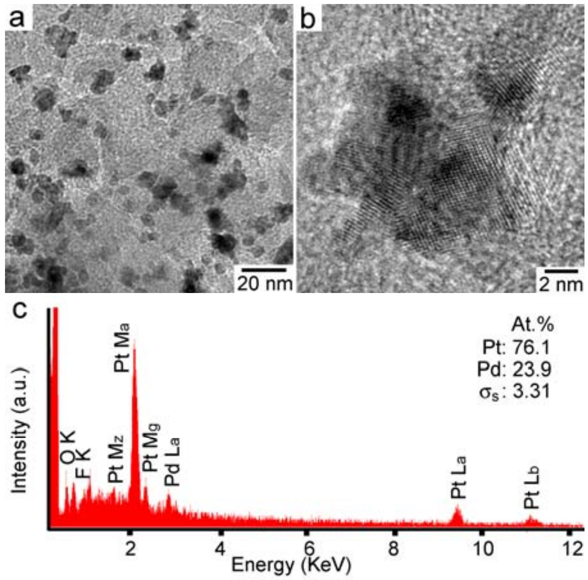

Figure S5. Representative (a) TEM, (b) HR-TEM image, and (c) EDX spectrum of carbon-supported Pt-on-Pd bimetallic nanoparticles after accelerated stability test (30,000 cycles).

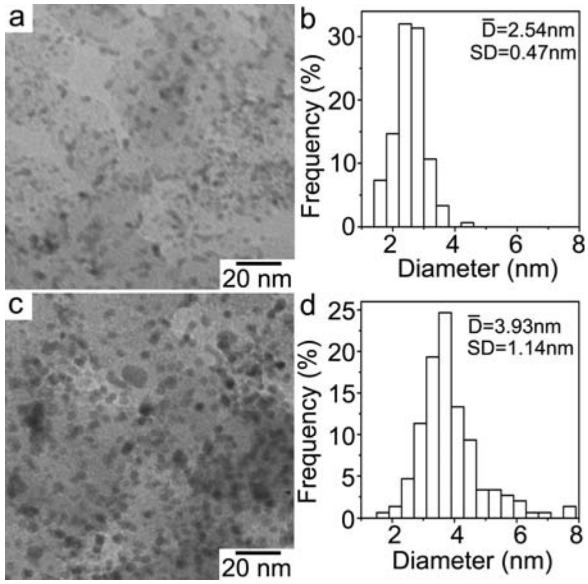

Figure S6. TEM images and particle size distribution analyses of Pt catalysts (E-TEK, 20wt.% Pt): (a, b) as-received and (c, d) after 30,000 CV cycles of accelerated stability test.